Enhanced Thermocatalytic Activity of Porous Yellow ZnO Nanoflakes: Defect- and Morphology-Induced Perspectives

Sunil M. Galani and Asit Baran Panda*[a]

Abstract: Herein, we report a simple and effective strategy for the synthesis of yellow ZnO (Y-ZnO) nanostructures with abundant oxygen vacancies on a large scale, through the sulfidation of ZnO followed by calcination. The developed strategy allows retention of the overall morphology of Y-ZnO compared with pristine ZnO and the extent of oxygen vacancies can be tuned. The influence of oxygen deficiencies, the extent of defect sites, and the morphology of ZnO on its solution-phase thermocatalytic activity has been eval-uated in the synthesis of 5-substituted-1H-tetrazoles with different nitriles and sodium azide. A reasonable enhance-ment in the reaction rate was achieved by using Y-ZnO nanoflakes (Y-ZnONFs) as a catalyst in place of pristine ZnONFs. The reaction was complete within 6 h at 110 °C with Y-ZnONFs, whereas it took 14 h at 120 °C with pristine ZnONFs. The catalyst is easy to recycle without a significant loss in catalytic activity.

Introduction

Nanostructured metal oxides are a highly important part of heterogeneous catalysts owing to their huge compositional, structural, and electronic variation and broad spectrum of properties and behaviors.[1] In the very early days, it was thought that the catalytic activity of oxide-based nanomaterials was mainly dependent on the surface area, but later it was confirmed that activity is also dependent on the size, shape, morphology, exposed facets, and importantly, on the crystal defects (both functional defects and oxygen vacancies) and the extent of these defects.[2,3]

ZnO is one of the most important low-cost, earth-abundant, sustainable, wide-bandgap semiconducting metal oxides, and has a wide range of applications.[4] ZnO is a key catalyst component in different gas-phase reactions, such as methanol synthesis, the water gas shift reaction, water and sulfur hydride dissociations, oxidation of CO, desulfurization processes, CO_2 activation processes, and the conversion of maleic anhydride to 1,4-butanediol.[5] It has also been used in different liquid-phase reactions.[6–11] However, in most reactions ZnO is used as co-catalyst or catalyst support; the use of pristine ZnO as a catalyst is rarely reported, most probably due to its lower activity.[8–11] Particularly for catalytic applications in the solution phase, pristine ZnO is widely used as a photocatalyst. Although it is a good photocatalyst, owing to its wide bandgap, its photocatalytic activity is limited to the UV range only, which limits its visible-light applications.[7–12] To improve its activity in both thermo- and photocatalysis, much effort has been made to develop size-, shape-, and morphology-selected ZnO nanocrystals.[13]

In general, the introduction of defect sites is one of the most important ways to enhance the catalytic activity of metal oxides. Self-doping, particularly defects from oxygen vacancies, is always advantageous for the improvement of properties compared with conventional doping systems, in which the introduction of impurities, that is, doped elements, may cause a reduction in catalytic activity.[2,14] Oxygen defects that induce improvements in the thermo-[15] and photocatalytic[16] activity of ZnO have been reported. However, in these samples the extent of oxygen deficiencies is very limited owing to the instability of oxygen vacancies under ambient conditions. For this reason, ZnO turns from white to yellow at high temperatures, owing to oxygen-vacancy-related defects, but gradually turns from yellow to white on cooling due to the instability of the oxygen vacancies generated at high temperatures.[17]

To overcome this problem and stabilize the maximum possible oxygen vacancies at room temperature, several physical methods, such as vacuum deoxidation, ball milling, cold plasma treatment, and electrospinning have been developed to generate stable oxygen vacancy sites in ZnO.[18] Although these methods have their own advantages, high cost, complicated steps, and uncontrollable oxygen deficiencies are the main drawbacks. In this regard, solution-based chemical methods are more attractive. However, very few chemical methods have been developed to produce stable oxygen-vacant ZnO systems.[19–25] The most popular method to achieve stable yellow ZnO with adequate oxygen vacancy sites is the calcination of zinc peroxide (ZnO_2).[19–21] Later, Xu et al. achieved oxygen-deficient yellow ZnO by heat treatment of a Zn(OH)F precursor.[22] Ullattil et al.[23] synthesized yellowish ZnO by calcination of zinc hydroxyl nitrate. However, the reported methods used corrosive HF and H_2O_2 and are morphology-specific, so it was not possible to synthesize oxygen-deficient ZnO with a

[a] *S. M. Galani, Dr. A. B. Panda*
Central Salt and Marine Chemicals Research Institute (CSIR-CSMCRI) and
CSMCRI-Academy of Scientific and Innovative Research (AcSIR)
G. B. Marg, Bhavnagar-364002, Gujarat (India)
E-mail: abpanda@csmcri.res.in

Supporting information and the ORCID identification number(s) for the au-thor(s) of this article can be found under:
https://doi.org/10.1002/asia.201801745.

desired morphology. However, these strategies offered the idea that it is possible to develop a simple protocol to generate stable oxygen vacancies in a ZnO structure through calcination of a specific precursor with an easy leaving group.

Adequate oxygen vacancies may also alter the ZnO band structure and make it visible-light active by narrowing the bandgap.[19–23] All the synthesized yellow ZnO showed improved visible-light-induced photocatalytic degradation of organic pollutants in the solution phase. However, the photocatalytic reaction mechanism is totally different to that of solution-phase thermocatalysis. The adequate oxygen vacancies in yellow ZnO may have adverse or positive effects in thermocatalysis. Unfortunately, to best of our knowledge, the effects of yellow ZnO with different oxygen vacancies in solution-phase thermocatalytic activity has not been studied. Thus, it is essential to develop a simple protocol for the synthesis of size- and shape-selective stable yellow ZnO with different oxygen vacancies and explore their corresponding effect in solution-phase thermocatalysis.

Herein we have developed a simple synthetic strategy for the preparation of yellow ZnO nanostructures with abundant oxygen vacancies by calcination of a ZnO/ZnS heterostructure, which was prepared by sulfidation of ZnO in a substitution reaction with Na_2S as the sulfur source. After calcination of ZnO/ZnS, no distinct morphological change was observed compared with pristine ZnO. The developed synthetic strategy not only offers an opportunity to synthesize morphology-selective oxygen-deficient yellow ZnO, but also allows controls of the degree of oxygen deficiency through control of the extent of sulfidation, that is, the amount of Na_2S, and this is the prime novelty of this work. We also applied this yellow ZnO in the solution-phase synthesis of 5-substituted-1H-tetrazoles form nitriles and sodium azide and studied the effects of defects and morphology on the catalytic activity. It was observed that yellow ZnO enhanced the rate of reaction reasonably and the reaction was complete in a short period of time (6 h), less than half that required for the same reaction with pristine ZnO (14 h), and also required a lower reaction temperature.

Results and Discussion

Catalyst characterization

Oxygen-deficient yellow ZnO was synthesized by the formation of a ZnO/ZnS heterostructure by sulfidation of pristine ZnO with different amounts of Na_2S as the sulfur source under ambient conditions, followed by calcination of the ZnO/ZnS heterostructure. Hereafter, the ZnO/ZnS heterostructures, obtained after sulfidation of pristine ZnO with various mole% of Na_2S, will be referred to as ZnO/ZnS structure-x (x = molar% of Na_2S used; structure = NFs (nanoflakes), NPs (nanoparticles), NRs (nanorods), or AGs (aggregates)). For example, ZnO/ZnS NFs synthesized with 30 mol% Na_2S is denoted as ZnO/ZnS NFs-30. Similarly, the yellow ZnO NFs obtained after calcination of the respective ZnO/ZnS heterostructure is denoted as Y-ZnO structure-x. For example, calcined material from ZnO/ZnS NFs-30 is denoted as Y-ZnO NFs-30.

Thermogravimetric analysis and sulfur estimation

In the first set of experiments, thermogravimetric analysis (TGA) of the ZnO/ZnS materials was performed to identify the calcination temperature at which ZnS decomposes completely to ZnO. Estimation of the sulfur content in ZnO/ZnS and the corresponding calcined Y-ZnO materials was also performed by using a CHNS analyzer to confirm the incorporation of sulfur and the degree of sulfur incorporated during sulfidation. The TGA curve for ZnO/ZnS-10 revealed a weight loss of nearly 1.5% within 200 °C, ascribed to the removal of trapped moisture, and a second weight loss of approximately 1.4% in the temperature range of 500 to 625 °C, ascribed to the decomposition of ZnS to ZnO (Figure S1 in the Supporting Information). Thus, all the ZnO/ZnS samples were calcined at 600 °C. CHNS analysis of the ZnO/ZnS samples showed a gradual increase in sulfur incorporation, as the molar ratio of Na_2S was increased. The corresponding calcined Y-ZnO samples showed the absence of any sulfur. Thus, CHNS analysis confirmed the incorporation of sulfur during sulfidation, which increased as the amount of Na_2S in the reaction mixture was increased, and the total decomposition of ZnS at 600 °C.

XRD pattern analysis

Powder XRD patterns were recorded to evaluate the phase of the synthesized materials at different stages of the reaction. Figure 1 shows the XRD pattern of pristine ZnO NFs, the ZnO/ZnS NFs-30 heterostructure, and Y-ZnO NFs-x (x = 10, 20, 30, 50) samples. The pristine ZnO NFs showed the presence of well-resolved X-ray diffraction peaks indexed to the hexagonal wurtzite structure of ZnO (JCPDS no. 36-1451; Figure 1a). In the XRD pattern of the ZnO/ZnS heterostructure, in addition to the wurtzite ZnO diffraction peaks, as observed for pristine ZnO, one low-intensity peak at $2\theta = 28.48°$ was observed (Figure 1b).
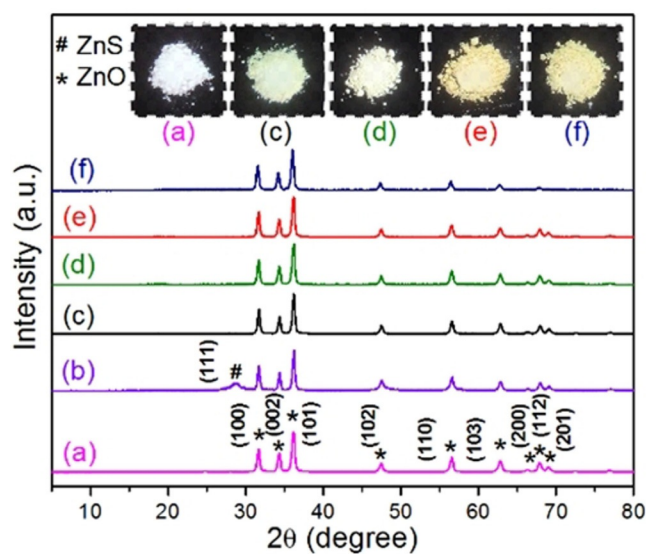

Figure 1. XRD patterns of a) pristine ZnO NFs, b) ZnO/ZnS NFs-30, c) Y-ZnO NFs-10, d) Y-ZnO NFs-20, e) Y-ZnO NFs-30, and f) Y-ZnO NFs-50. Inset: Digital photograph of the corresponding ZnO samples.

The additional peak can be identified as the (111) plane of cubic zinc blende ZnS phase and indicates the formation of ZnS on the ZnO surface during sulfidation through ion-exchange with Na_2S. Note that the peak intensity of the (111) plane of cubic zinc blende ZnS phase of the ZnO/ZnS samples obtained after sulfidation with different amounts of Na_2S varied. It gradually increased as the amount of Na_2S was increased, which indicated an increase in the degree of sulfidation (Figure S2). Conversely, the XRD pattern of the sample obtained after calcination of the ZnO/ZnS heterostructure showed the presence of diffraction peaks for wurtzite ZnO only, similar to that of pristine ZnO; the peak at $2\theta = 28.48°$, assigned to ZnS, disappeared (Figure 1c–f). No such distinct difference between the XRD patterns of pristine ZnO and Na_2S-treated ZnO was observed. The only identifiable difference is their physical appearance: pristine ZnO is white, whereas the Na_2S-treated ZnO was yellow with varying intensities, and the color intensity increased as the degree of sulfidation increased (Figure 1, inset). Y-ZnONFs-10 is light yellow, whereas Y-ZnONFs-30 is a brighter yellow. No distinct color change was identified between Y-ZnONFs-30 and Y-ZnONFs-50, and the color intensity of both samples was almost identical (Figure 1, inset). ZnO with various morphologies also showed an identical characteristic change in the XRD pattern and physical appearance compared with ZnONFs (Figure S3). This phenomenon indicated that some surface structural changes took place in the ZnO surface during the calcination of ZnO/ZnS heterostructures, due to the decomposition of surface ZnS. This surface structural change is primarily responsible for the color change, with the overall crystal structure kept intact. However, it is not possible to identify the specific surface structural changes from the XRD patterns.

SEM and TEM analysis

The SEM image of pristine ZnONFs revealed the formation of a flake-like structure with an average length of 2 to 3 µm and width of 400 to 600 nm, and the flakes are quite thin and porous (Figure 2a). The flakes are random and no specific arrangement of flakes was identified. After reaction of pristine ZnO with Na_2S (ZnO/ZnS), that is, sulfide formation, the flake structure remained intact and resulted in a nearly identical flake structure with an overall morphology that was very similar to that of pristine ZnO. However, the flake surfaces became smoother and pores disappeared (Figure 2b). During sulfidation through ion-exchange, hexagonal ZnO was transformed to cubic ZnS. This phase transformation may generate strain in the system and result in the destruction of the system, which is a probable reason for pore blockage. After calcination, that is, decomposition of ZnS, the pores were regenerated. The overall morphology of Y-ZnONFs is more-or-less identical to that of pristine ZnONFs (Figure 2c). The SEM images of Y-ZnO with other morphologies also revealed retention of the overall morphology of the respective pristine ZnO morphology (Figure S4–S6). The TEM image of Y-ZnONFs-30 confirmed the formation of a porous flake structure (Figure 2d). The corresponding magnified image shows the presence of distinct pores with
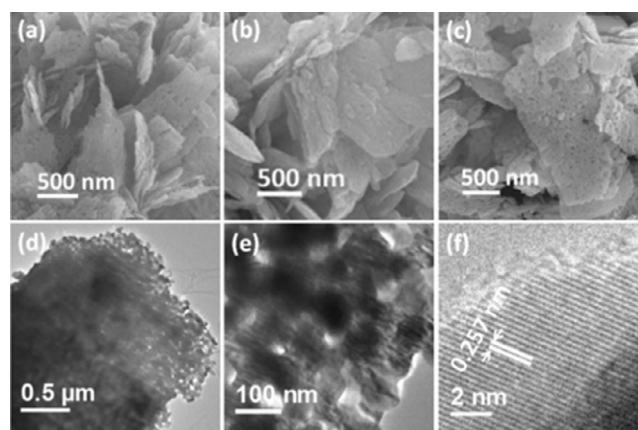

Figure 2. SEM images of a) pristine ZnONFs, b) ZnO/ZnS-30 NFs, and c) the corresponding Y-ZnONFs-30. d,e) TEM and f) HR-TEM images of Y-ZnONFs-30.

a broad pore-size distribution in the range of 20 to 60 nm (Figure 2e). The respective high-resolution TEM (HR-TEM) image shows the presence of distinct lattice fringes, which confirmed the highly crystalline nature of the synthesized ZnO materials. The lattice fringe spacing of 0.257 nm can be ascribed to the *d*-spacing between the (002) planes of hexagonal wurtzite ZnO, and supports the XRD results (Figure 2f). The EDX spectra of Y-ZnO, from both the TEM and SEM images, also indicated the absence of sulfur and confirmed the complete decomposition of ZnS in the ZnO/ZnS heterostructures during calcination (Figure S7).

Raman spectra analysis

To confirm the structure and surface composition of the synthesized Y-ZnO, Raman spectroscopic analysis was performed. Figure 3 shows the Raman spectra of synthesized ZnO samples in the range of 200 to 700 cm^{-1}. The Raman spectrum of pristine ZnONFs showed the presence of one intense peak at 435 cm^{-1}, one low-intensity peak at 330 cm^{-1}, and a small, broad hump at around 577 cm^{-1} (Figure 3a). The intense peak at 435 cm^{-1} can be assigned to the typical Raman vibration modes of wurtzite ZnO, the peak at 330 cm^{-1} is attributed to multiple phonon scattering processes, and the broad hump at 577 cm^{-1} is associated with the oxygen vacancy sites.[22,23] The Raman spectra of Y-ZnO, obtained after calcination of respective sulfidation product (ZnO/ZnS), revealed the presence of all the peaks observed for pristine ZnO. However, the peak intensity at 577 cm^{-1}, assigned to the oxygen vacancy sites, varied and gradually increased as the degree of sulfidation in ZnO/ZnS increased, that is, the amount of Na_2S used during sulfidation. This observation showed that the extent of oxygen vacancies is directly related to the degree of sulfidation. With the increase in sulfidation, the extent of oxygen vacancies increased. Therefore, Y-ZnONFs-10 is light yellow in color due to the presence of comparatively fewer oxygen vacancy sites, whereas Y-ZnONFs-30 is an intense yellow color owing to the presence of a larger number of oxygen vacancy sites. However, the intensity of the peak at 577 cm^{-1} for Y-ZnONFs-30 is simi-
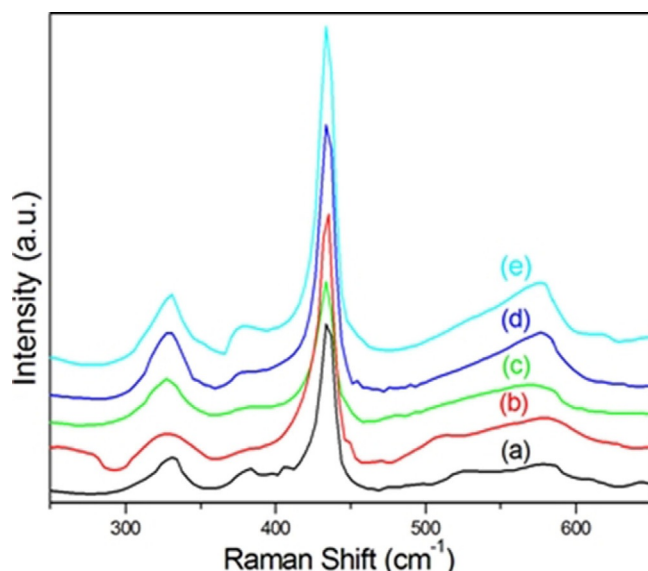
Figure 3. Raman spectra of a) pristine ZnONFs, b) Y-ZnONFs-10, c) Y-ZnONFs-20, d) Y-ZnONFs-30, and e) Y-ZnONFs-50.

lar to that of Y-ZnONFs-50, which indicates that the latter has a surface saturation of oxygen vacancy sites identical to Y-ZnONFs-30. ZnO with varying morphologies, obtained after sulfidation with 30% Na_2S, also showed similar Raman spectra.

XPS analysis

Further XPS analysis was performed to confirm the composition and get more insight into the oxygen vacancies. Before analysis, calibrations of all the spectra were performed with C 1s peak located at 284.50 eV. Figure 4a shows the wide-survey elemental spectrum of Y-ZnONFs-30. The survey spectrum clearly reveals the presence of oxygen and zinc only, and confirms the total decomposition of ZnS. The corresponding high-resolution core-level Zn 2p spectrum in the binding
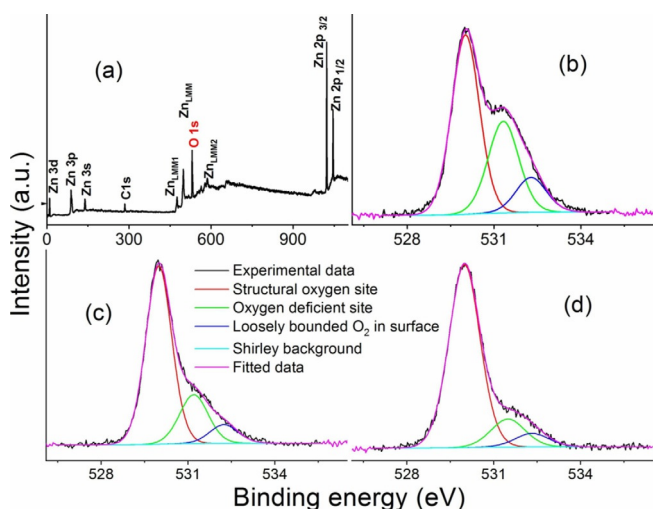
energy range of 1010 to 1055 eV shows the presence of two distinct peaks at 1021.9 and 1044.8 eV, indexed to Zn 2p$_{3/2}$ and Zn 2p$_{1/2}$, and confirms the presence of Zn^{2+} (Figure S8). However, high-resolution O 1s spectra are more important to get detailed information about the environment and status of the surface oxygen and respective vacancies. Figure 4b–d shows the high-resolution O 1s spectra of Y-ZnONFs-30, Y-ZnONFs-10, and pristine ZnONFs. The deconvoluted high-resolution O 1s spectra of all samples showed three distinctly identifiable peaks at about 530, 531.5, and 532.3 eV. The high-intensity peak at lower energy is usually assigned to O^{2-} ions in a hexagonal Zn^{2+} ion array in wurtzite ZnO (i.e., structural O^{2-} ions). The low-intensity peak at higher binding energy is associated with loosely bound oxygen in the ZnO surface, whereas the peak at medium binding energy (i.e., 531.5 eV) can be assigned to O^{2-} ions present in the oxygen-deficient sites of the ZnO surface.[19, 22, 24] In all three spectra, the ratio of peak intensity and the corresponding area of the peaks associated with structural O^{2-} ions and loosely bound oxygen atoms were almost identical. However, the peak intensity and the corresponding area of the peak at 531.5 eV associated with O^{2-} ions in the oxygen-deficient sites varied, and was much higher for Y-ZnONFs-30. The area ratios of the peaks at 530 and 531.5 eV for Y-ZnONFs-30, Y-ZnONFs-10, and pristine ZnONFs were 0.56, 0.3, and 0.17, respectively. The XPS results confirmed that the oxygen vacancy sites have a direct relationship to the degree of sulfidation, and Y-ZnONFs-30 contains many more oxygen vacancy sites than pristine ZnONFs. Thus, the XPS result supports the results obtained from the Raman spectra.

Textural and microstructural analysis

Next, it was imperative to determine the probable overall textural and microstructural changes in bare ZnO flakes and Y-ZnO flakes because these are the limiting parameters of catalytic activity, and were evaluated by using nitrogen adsorption/desorption analysis. The nitrogen sorption isotherms for both samples correspond to type II and the hysteresis loops are almost H3 type, ascribed to aggregated particles (Figure S9). The pore-size distribution curve, obtained from the desorption part of the nitrogen sorption isotherm, confirmed the presence of a broad pore-size distribution, in the range of 10 to 90 nm with an average pore size of 50 nm, which supports the result obtained from TEM analysis. The total BET surface area of the bare ZnO flakes was 13 $m^2 g^{-1}$ with a total pore volume of 0.11 $cc\,g^{-1}$, whereas the total BET surface area and total pore volume of Y-ZnONFs-30 were 10 $m^2 g^{-1}$ and 0.098 $cc\,g^{-1}$, respectively. Thus, nitrogen sorption analysis indicated that no distinct textural or microstructural changes took place during sulfidation followed by calcination.

Diffuse reflectance spectroscopy (DRS) analysis

It is well established that oxygen vacancy sites in ZnO have a direct effect on the corresponding band structure.[19–23] Thus, the optical properties were measured by using UV/Vis DRS for further confirmation of the presence of oxygen vacancies and
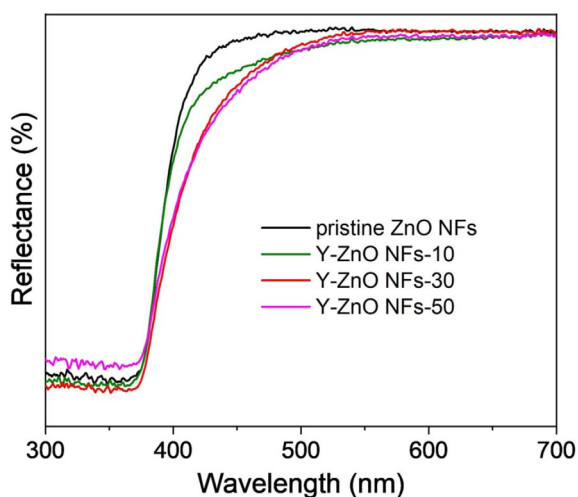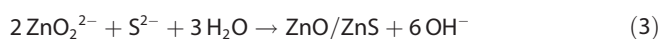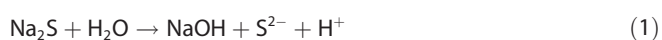

Figure 4. a) Survey XPS spectrum of Y-ZnONFs-30. O 1s spectra of b) Y-ZnONFs-30, c) Y-ZnONFs-10, and d) pristine ZnONFs.

Figure 5. UV/Vis DRS spectra of the synthesized samples.

the effect of the degree of oxygen vacancies in the band structure. From Figure 5, it is noted that the absorption edge of all the Y-ZnONFs samples shifted towards longer wavelengths (redshifted) compared with pristine ZnONFs. Furthermore, it also showed that, with an increase in the degree of sulfidation, that is, the number of oxygen vacancy sites, a gradual redshift in the absorption edge was observed. However, the adsorption edge of Y-ZnONFs-30 and Y-ZnONFs-50 appeared very close. This observation revealed the saturation of oxygen vacancy sites in Y-ZnONFs-30 and supports both the Raman and XPS analyses.

Formation mechanism

The overall strategy for the synthesis of morphology-selective oxygen-deficient Y-ZnO is based on the synthesis of crystalline ZnO with the desired morphology, formation of a ZnO/ZnS heterostructure through sulfidation of the synthesized ZnO with Na_2S, and calcination of the ZnO/ZnS heterostructure to give the desired oxygen-deficient Y-ZnO with more-or-less identical morphology to that of the pristine ZnO. Sulfidation took place at the ZnO surface through an ion-exchange mechanism.[26] After calcination in air, ZnS on the ZnO surface decomposed and formed ZnO.[27] During calcination, the sulfur in ZnS was oxidized and removed from the surface as SO_2. Simultaneously, the zinc was oxidized to ZnO by an exchange reaction between oxygen and sulfur. The reactions took place during the overall transformation of pristine ZnO to oxygen-deficient Y-ZnO, as shown in Reactions (1)–(4):

$$Na_2S + H_2O \rightarrow NaOH + S^{2-} + H^+ \qquad (1)$$

$$ZnO + 2\,OH^- \rightarrow ZnO_2{}^{2-} + H_2O \qquad (2)$$

$$2\,ZnO_2{}^{2-} + S^{2-} + 3\,H_2O \rightarrow ZnO/ZnS + 6\,OH^- \qquad (3)$$

$$2\,ZnS\ (ZnO/ZnS) + 3\,O_2 \xrightarrow{\Delta} 2\,ZnO + 2\,SO_2 \uparrow \qquad (4)$$

However, the rate of desulfidation (removal of SO_2) is much faster than the formation of ZnO, that is, reoxidation of zinc, which generates oxygen-deficient sites in the surface and results in a yellow color.[28] Under these reaction conditions, sulfidation took place only on the surface. Thus, after saturation of the ZnO surface by ZnS, further sulfidation of the inner core was negligible and the degree of sulfidation remained constant. As a result, the degree of oxygen vacancies remains almost the same.

Catalytic applications

Nitrogen-rich tetrazoles are very important heteroaromatic compounds and are used in a large number of fields, such as different biomedical applications, pharmaceuticals, agriculture, as anti-foggants in photographic materials, information recording systems, propellants, and explosives.[29] Traditionally, tetrazoles are synthesized from the catalytic reaction of nitriles and azide through [3+2] cycloaddition by using corrosive concentrated Lewis acids. Later, different metal complexes, inorganic salts and Zn/Al hydrotalcite (HT), Zn hydroxyapatite, ZnO and ZnS, have been developed as homogeneous and heterogeneous catalysts.[30, 31] However, homogeneous catalysts are not reusable and the homogeneous and heterogeneous catalysts both need longer reaction times, a large excess of sodium azide (3:1 azide/nitrile), and high temperatures. Even so, the yields are not satisfactory most of the time. Recently, we used porous ZnO flakes for the synthesis of 5-substituted-1*H*-tetrazoles, which was able to give a satisfactory yield (90% for 5-*p*-bromophenyl-1*H*-tetrazole) with a reduced amount of azide (1.2 equiv).[10] However, the reaction time and temperature were quite high (14 h, 120 °C), and should be reduced. A study of the reaction pathway indicated that adsorption of nitrile on the Zn sites on the ZnO surface facilitates the reaction progress.[10] It is expected that defects in ZnO may facilitate the adsorption of nitrile on the ZnO surface and accelerate the rate of the reaction.

Inspired by this hypothesis, we used synthesized Y-ZnO structures with different morphologies and different degrees of surface defects to understand the effect of the surface defects, the corresponding degree of defects, and the morphology on the rate of reaction. In the first set of reactions, all the synthesized ZnONFs, that is, pristine and Y-ZnO with different degrees of oxygen-deficient sites, were applied in the synthesis of 5-phenyl 1*H*-tetrazole, with 1.2 equivalents of sodium azide with respect to benzonitrile, in DMF as the solvent. The reactions were performed at 120 °C for 14 h. All reactions were ended with 100% selectivity of the desired product and more-or-less identical isolated yields of 90%. The results confirmed that generation of oxygen-deficient sites did not reduce the catalytic activity to that of pristine ZnONFs. Next, we repeated the reactions for 6 h and obtained a range of yields with the different samples. We are delighted to report that both Y-ZnONFs-30 and Y-ZnONFs-50 gave a maximum yield of 89%, very close to the yield obtained after a reaction time of 14 h (Table 1). Conversely, Y-ZnONFs-20, Y-ZnONFs-10, and pristine ZnONFs gave 84, 72, and 57% isolated yields of the desired

Table 1. Optimization of the synthesis of 5-phenyl-1*H*-tetrazole with different synthesized ZnO catalysts.[a]
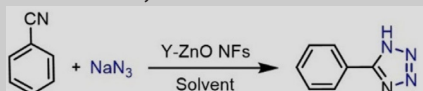
Entry	Catalyst	T [°C]	t [h]	Conv. [%]	Isolated yield [%]
1	ZnO NFs	120	6	61	57
		120	12	94	90
2	Y-ZnO NFs-10	120	6	78	72
3	Y-ZnO NFs-20	120	6	90	84
4	Y-ZnO NFs-30	120	6	93	89
		110	6	93	89
5	Y-ZnO NFs-50	120	6	93	89
6	Y-ZnO NRs-30	120	6	82	78
7	Y-ZnO NPs-30	120	6	83	79
8	Y-ZnO AGs-30	120	6	71	67

[a] Reaction conditions: Benzonitrile (1.0 mmol, 1 equiv), sodium azide (1.2 mmol, 1.2 equiv), DMF (2 mL), catalyst (30 mg).

product. This result confirmed that the oxygen-deficient sites play a definite role in the rate of the reaction; an increase in the degree of defect sites increased the yield after a reaction time of 6 h. The oxygen-deficient Zn sites of ZnO facilitate the chemisorption of nitrile on the surface and accelerate the rate of reaction. With an increase in the oxygen vacancies (the active sites), nitrile adsorption increased, which in turn increased the rate of reaction and the reaction was complete in a short period of time. Due to the presence of almost identical amounts of oxygen-deficient sites in Y-ZnO NFs-30 and Y-ZnO NFs-50, as identified by Raman and DRS spectroscopic analyses, both samples showed similar catalytic activity. Thus, the results support our hypothesis. We repeated the reaction with Y-ZnO NP/NR/AG-30 as the catalyst but obtained a reduced yield compared with Y-ZnO NFs-30 (Table 1). These results further confirmed the morphology-induced catalytic activity of oxygen-deficient ZnO. The nonporous nature of the NRs, the thick porous NPs, and aggregation of the nanoparticles reduced the available active sites on ZnO, and are the probable prime origin of the reduced catalytic activity.

Next, we selected Y-ZnO NFs-30, as an active catalyst in the synthesis of tetrazole, for further detailed investigations. To understand the exact time required to complete the reaction, the reaction was performed at 120 °C with different reaction times (Figure S10). From the corresponding reaction profile, it is evident that the reactions proceeded at a faster rate initially; a 78 % yield was obtained within 4 h. Subsequently, the reaction became slower: an 89 % yield was observed after 6 h, which remained almost constant up to 10 h. The reaction temperature was also optimized by performing the reaction at different temperatures. Happily, we can report that reaction also proceed smoothly even at 110 °C with an identical yield, and that further reduction in the temperature significantly affected the yield (Figure S11). No such distinct change in yield was observed after an increase in the amount of azide. DMF was found to be the best solvent for better yields (Table S1). Note

that, in the absence of catalyst, no product formation was observed. The optimal amount of catalyst was determined to be 30 mg of catalyst to 1 mmol nitrile.

After this exciting result for the synthesis of 5-phenyl-1*H*-tetrazoles in 90 % yield at 110 °C after 6 h, the scope of the catalyst was explored for several structurally different nitriles. Although the activity varied according to the substrate and needed separate optimization for individual substrates, we were able to get good yields of different tetrazoles successfully just by optimizing the reaction time, which proved the broad applicability of Y-ZnO NFs-30 as a heterogeneous catalyst (Table 2). All the substituted aryl nitriles gave excellent yields. Halogen (Cl, Br) and acid (COOH)-substituted aryl nitriles gave greater than 90 % isolated yields, whereas aldehyde (CHO), cyanide (CN), and hydroxyl (OH)-substituted aryl nitriles gave slightly reduced yields (60–70 %).

Table 2. Synthesis of 5-substituted 1*H*-tetrazole derivatives.[a]
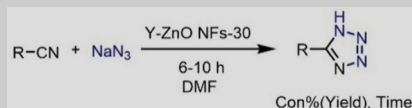

[a] Reaction conditions: Benzonitrile (1.0 mmol, 1 equiv), sodium azide (1.2 mmol, 1.2 equiv), catalyst Y-ZnO NFs-30 (30 mg), DMF (2 mL).

For heterogeneous catalysts, recyclability is a crucial issue. There is a high probability of a drop in the catalytic activity of Y-ZnO owing to a reduction in oxygen-deficient sites under the reaction condition. Thus, the recyclability of Y-ZnO NFs-30 was tested in the synthesis of 5-phenyl-1*H*-tetrazole over five consecutive runs. After completion of the reaction in each cycle, the catalyst was separated by simple centrifugation, washed well with ethyl acetate, dried overnight in the oven, and used in the next cycle. Figure S12 summarizes the conversion and isolated yield after each cycle. More importantly, note that after the fifth cycle a negligible decrease in yield was observed (79 % isolated yield). A structural and morphological characterization showed that the catalyst was stable even after the fifth cycle and the overall characteristics remained intact (Figures S13–14). Even the physical appearance (yellow color) remained intact (Figure S15). However, in the IR spectrum of the used catalyst, the presence of surface-adsorbed nitrile was

identified. This is the probable origin of the minor reduction in catalytic activity (Figure S16).

Table S2 presents a comparison of the catalytic activity of different reported heterogeneous catalysts, including ZnO nanostructure, with Y-ZnO NFs-30 in the synthesis of 5-phenyl-1*H*-tetrazole with benzonitrile and NaN₃. It is evident that Y-ZnO NFs-30 showed superior catalytic activity based on isolated yield, reaction time (less than half the lowest reported time), the amount of sodium azide, and the temperature, and thus is advantageous to use.

It is difficult to study the reaction mechanism and the corresponding pathway for heterogeneously catalyzed reactions. However, there are reports on mechanistic studies for the synthesis of tetrazole by using nitrile and azide with transition-metal-based (Zn, Co) homogeneous catalysts. According to the reports, nitrile coordinates to the transition-metal ion (Zn^{2+}, Co^{2+}), followed by nucleophilic attack by the azide and subsequent cycloaddition.[10,31] The coordination step reduced the active energy (approximately 5–6 Kcal mol^{-1}) and is presumed to be the rate-determining step. As per our experimental findings, we believe that the ZnO-catalyzed reaction herein also follows the same pathway. The first step is the chemisorption of nitriles on a Zn site on the ZnO surface, then nucleophilic attack of the azide followed by subsequent cycloaddition and desorption of the desired product. With pristine ZnO, the reaction proceeds slowly due to the slow chemisorption step, and requires a longer reaction time. Conversely Zn at oxygen-deficient sites in Y-ZnO facilitates the chemisorption of nitriles and assists the progress of the reaction. Thus, the time required for reaction completion is highly dependent on the number of oxygen-deficient sites in Y-ZnO. We have proposed a probable reaction pathway based on the experimental findings (Scheme 1).
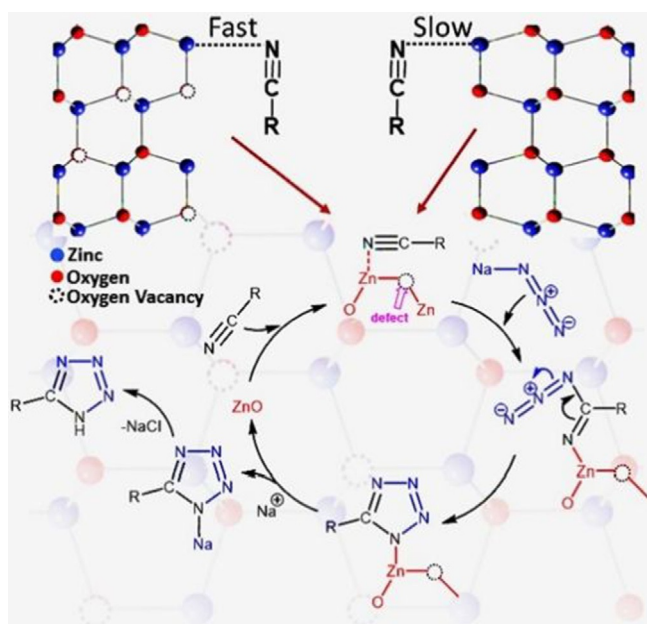
Scheme 1. Schematic representation of the likely reaction path in the synthesis of 5-substituted-1*H*-tetrazole, in the presence of Y-ZnO with abundant oxygen vacancies as the heterogeneous catalyst.

Conclusions

We have successfully synthesized yellow ZnO (Y-ZnO) with abundant oxygen vacancies by sulfidation and calcination of a pristine ZnO with the desired morphology. The degree of sulfidation can be tuned simply by varying the extent of sulfidation. During calcination of the ZnO/ZnS heterostructure, the rate of desulfidation is much faster than ZnO formation, which generates oxygen-deficient sites. Catalytic activity experiments revealed the influence of morphology and the degree of oxygen vacancies of Y-ZnO on the solution-phase thermocatalytic activity. It was observed that oxygen-deficient sites enhanced the rate of reaction with different nitriles and sodium azide to 5-substituted-1*H*-tetrazoles. Catalyst Y-ZnO NFs-30 showed superior activity and the reaction was complete in a very short period of time (6 h) at low temperature (110 °C) with respect to pristine ZnO NFs. The Y-ZnO is easily recycled and can perform at least five consecutive catalytic cycles without a significant loss in catalytic activity. Synthesized Y-ZnO with varying morphologies and defect degrees can be applied in a large variety of reactions for improved results.

Experimental Section

Materials

Zinc nitrate hexahydrate [$Zn(NO_3)_2 \cdot 6H_2O$] was purchased from RanKem (Ranbaxy), India; ammonium carbonate (NH_4HCO_3 and $NH_2CO_2NH_4$, 95.3 %), triethanolamine ($C_6H_{15}NO_3$; TEA), $Na_2S \cdot 9H_2O$, bulk ZnO, and ammonium hydroxide (NH_4OH) were purchased from S. D. Fine-Chem., India. All purchased analytical-grade chemicals were used without further purification. All organic reagents were purchased from Sigma–Aldrich, USA. Water from a Millipore water purifier with a resistivity of 18 MΩ cm^{-1} was used.

Synthetic procedures for ZnO nanostructures with different morphologies

Porous ZnO nanoflakes (ZnO NFs)

In a typical process, TEA (3 mL) was mixed with deionized water (15 mL) and aqueous $Zn(NO_3)_2 \cdot 6H_2O$ (10 mL, 3.0 g, 10.07 mmol) was added slowly to this mixture with stirring at RT. Then, aqueous ammonium carbonate (15 mL, 4.5 g) was added dropwise to the solution and the final mixture was stirred for 6 h at RT. Finally, a portion of the solution (33 mL) was placed in a 50 mL Teflon-lined autoclave, sealed properly, and kept in a preheated oven at 150 °C for 6 h. The resultant white precipitate (obtained on cooling) was collected, thoroughly washed several times with deionized water, and dried overnight at 70 °C in an oven. The dried product was calcined in air at 500 °C for 3 h.

Aggregated ZnO nanoparticles (ZnO AGs)

In a typical process, dilute aqueous NaOH was added dropwise to aqueous $Zn(NO_3)_2 \cdot 6H_2O$ (50 mL, 5.0 g) with stirring at RT until a pH of 10 was reached, then the stirring was continued for further 30 min. The obtained white precipitate was collected by centrifugation, washed thoroughly with deionized water several times, and dried overnight at 70 °C in an oven. The obtained precursor material was calcined in air at 500 °C for 3 h.

Separately assembled porous 3D ZnO nanoplates (ZnONPs) and ZnO nanorods (ZnONRs) were prepared by following previously reported methods.[9, 32]

Synthesis of yellow ZnO nanostructures

Yellow ZnO with defect sites was synthesized by sulfidation of pristine ZnO with Na_2S as sulfur source to give a ZnO/ZnS heterostructure, followed by calcination of the ZnO/ZnS heterostructure under ambient conditions. In a typical reaction procedure, synthesized ZnO nanostructures (200 mg) were dispersed in water (20 mL) and different amounts of Na_2S, (10, 20, 30, 50 mol% relative to ZnO) was dissolved in water (40 mL). The two solutions were mixed and heated at 60 °C for 2 h with constant stirring. Finally, the product was washed three or four times with deionized water and then methanol, and dried overnight at 70 °C. Finally, the dried ZnO/ZnS heterostructures were calcined at 600 °C for 3 h.

Detailed synthetic procedure for the synthesis of tetrazole

In a typical synthesis of 5-phenyl 1H-tetrazole, ZnO (0.03 g), benzonitrile (1.0 mmol), sodium azide (1.2 mmol), and DMF (2 mL) were placed in a round-bottom flask, then transferred to an oil bath, fitted with a reflux condenser, and heated at 110 °C for 6 h with stirring (600 rpm). During the heat treatment, the progress of the reaction was monitored by using thin-layer chromatography (TLC). After reaction completion, ethyl acetate (20 mL) was added to the reaction mixture and the catalyst was separated by centrifugation. Next, HCl (20 mL, 3 N) and ethyl acetate (20 mL) were added to the reaction mixture with vigorous stirring for 15 min, then left to stand for a further 10 min. The resultant organic layer was separated and the aqueous layer was again treated with ethyl acetate (20 mL), and the separation process was repeated a further three times. The combined extracted ethyl acetate fractions were dried over anhydrous $MgSO_4$, then concentrated to obtain the tetrazole products. All products were characterized by using ^1H and ^{13}C NMR spectroscopy and FTIR analysis, which were in agreement with literature reports. The separated catalyst was washed with acetone and ethyl acetate and reused.

Conflict of interest

The authors declare no conflict of interest.

[1] a) C. T. Campbell, J. Sauer, *Chem. Rev.* **2013**, *113*, 3859–3862; b) A. R. Puigdollers, P. Schlexer, S. Tosoni, G. Pacchioni, *ACS Catal.* **2017**, *7*, 6493–6513.

[2] J. Jia, C. Qian, Y. Dong, Y. F. Li, H. Wang, M. Ghoussoub, K. T. Butler, A. Walsh, G. A. Ozin, *Chem. Soc. Rev.* **2017**, *46*, 4631–4644.

[3] a) N. Sutradhar, A. K. Biswas, S. K. Pahari, B. Ganguly, A. B. Panda, *Chem. Commun.* **2014**, *50*, 11529–11532; b) P. Pal, S. K. Pahari, A. K. Giri, S. Pal, H. C. Bajaj, A. B. Panda, *J. Mater. Chem. A* **2013**, *1*, 10251–10258; c) M.-Q. Yang, M. Gao, M. Hong, G. W. Ho, *Adv. Mater.* **2018**, *30*, 1802894; d) M.-Q. Yang, J. Wang, H. Wu, G. W. Ho, *Small* **2018**, *14*, 1703323.

[4] a) A. Kołodziejczak-Radzimska, T. Jesionowski, *Materials* **2014**, *7*, 2833–2881; b) A. Hatamie, A. Khan, M. Golabi, A. P. Turner, V. Beni, W. C. Mak, A. Sadollahkhani, H. Alnoor, B. Zargar, S. Bano, O. Nur, M. Willander, *Langmuir* **2015**, *31*, 10913–10921; c) F.-X. Liang, Y. Gao, C. Xie, X.-W. Tong, Z.-J. Li, L.-B. Luo, *J. Mater. Chem. C* **2018**, *6*, 3815–3833.

[5] a) S. Kuld, M. Thorhauge, H. Falsig, C. F. Elkjær, S. Helveg, I. Chorkendorff, J. Sehested, *Science* **2016**, *352*, 969–974; b) B. Meyer, D. Marx, O. Dulub, U. Diebold, M. Kunat, D. Langenberg, C. Wçll, *Angew. Chem. Int. Ed.* **2004**, *43*, 6641–6645; *Angew. Chem.* **2004**, *116*, 6809–6814; c) Y. Feng, J. Mi, J. Wu, J. Shangguan, H. Fan, *Energy Fuels* **2017**, *31*, 1015–1022; d) W.-D. Oh, J. Lei, A. Veksha, A. Giannis, G. Lisak, V. W.-C. Chang, X. Hu, T.-T. Lim, *Fuel* **2018**, *211*, 591–599; e) X. Gu, C. Huanga, W. Li, *Catal. Sci. Technol.* **2017**, *7*, 4294–4301; f) D. Ma, Q. Wang, T. Li, Z. Tang, G. Yang, C. He, Z. Lu, *J. Mater. Chem. C* **2015**, *3*, 9964–9972; g) S. G. Girol, T. Strunskus, M. Muhler, C. Wöll, *J. Phys. Chem. B* **2004**, *108*, 13736–13745.

[6] A. F. Shojaei, K. Tabatabaeian, M. A. Zanjanchi, H. F. Moafi, N. Modirpanah, *J. Chem. Sci.* **2015**, *127*, 481–491.

[7] a) S. K. Johnston, N. Cherkasova, E. P. Barrado, A. Aho, D. Y. Murzin, A. O. Ibhadon, M. G. Francesconi, *Appl. Catal. A* **2017**, *544*, 40–45; b) X. Song, H. Sun, X. Cao, Z. Wang, D. Zhao, J. Sun, H. Zhang, X. Li, *RSC Adv.* **2016**, *6*, 112451–112454; c) Y. Li, Y. Zheng, L. Wang, Z. Fu, *ChemCatChem* **2017**, *9*, 1960–1968.

[8] A. K. Giri, A. Sinhamahapatra, S. Prakash, J. Chaudhari, V. K. Shahi, A. B. Panda, *J. Mater. Chem. A* **2013**, *1*, 814–822.

[9] A. K. Giri, A. Saha, A. Mondal, S. C. Ghosh, S. Kundu, A. B. Panda, *RSC Adv.* **2015**, *5*, 102134–102142.

[10] A. Sinhamahapatra, A. K. Giri, P. Pal, S. K. Pahari, H. C. Bajaj, A. B. Panda, *J. Mater. Chem.* **2012**, *22*, 17227–17235.

[11] a) B. V. Kumar, H. S. B. Naik, D. K. Girija, *J. Chem. Sci.* **2011**, *123*, 615–621; b) M. Hosseini-Sarvari, H. Sharghi, *J. Org. Chem.* **2006**, *71*, 6652–6654; c) A. Nagvenkar, S. Naik, J. Fernandes, *Catal. Commun.* **2015**, *65*, 20–23; d) R. Tayebee, A. H. Nasr, S. Rabiee, E. Adibi, *Ind. Eng. Chem. Res.* **2013**, *52*, 9538–9543.

[12] a) C. B. Ong, L. Y. Ng, A. W. Mohammad, *Renewable Sustainable Energy Rev.* **2018**, *81*, 536–551; b) K. M. Lee, C. W. Lai, K. S. Ngai, J. C. Juan, *Water Res.* **2016**, *88*, 428–448; c) S. B. A. Hamid, S. J. Teh, C. W. Lai, *Catalysts* **2017**, *7*, 93–106.

[13] a) Y. Sun, L. Chen, Y. Bao, Y. Zhang, J. Wang, M. Fu, J. Wu, D. Ye, *Catalysts* **2016**, *6*, 188; b) Y. Zheng, C. Chen, Y. Zhan, X. Lin, Q. Zheng, K. Wei, J. Zhu, Y. Zhu, *Inorg. Chem.* **2007**, *46*, 6675–6682; c) N. Talebian, S. M. Amininezhad, M. Doudi, *J. Photochem. Photobiol. B* **2013**, *120*, 66–73; d) E. P. Babu, A. Subastri, A. Suyavaran, K. Premkumar, V. Sujatha, B. Aristatile, G. M. Alshammari, V. Dharuman, C. Thirunavukkarasu, *Sci. Rep.* **2017**, *7*, 4203–4214.

[14] a) D. Chen, C. Chen, Z. M. Baiyee, Z. Shao, F. Ciucci, *Chem. Rev.* **2015**, *115*, 9869–9921; b) L. Wang, Y. Yu, H. He, Y. Zhang, X. Qin, B. Wang, *Sci. Rep.* **2017**, *7*, 12845–12855; c) A. Saha, A. Sinhamahapatra, T.-H. Kang, S. C. Ghosh, J.-S. Yu, A. B. Panda, *Nanoscale* **2017**, *9*, 17029–17036.

[15] a) M. V. Morales, E. A. -Nieto, A. I. -Juez, I. R. -Ramos, A. G. -Ruiz, *ChemSusChem* **2015**, *8*, 2223–2230; b) C. Drouilly, J.-M. Krafft, F. Averseng, H. L. -Pernot, D. B. -Bachic, C. Chizallet, V. Lecocqc, G. Costentina, *Appl. Catal. A* **2013**, *453*, 121–129; c) S. Polarz, J. Strunk, V. Ischenko, M. W. E. Berg, O. Hinrichsen, M. Muhler, M. Driess, *Angew. Chem. Int. Ed.* **2006**, *45*, 2965–2969; *Angew. Chem.* **2006**, *118*, 3031–3035; d) M.-H. Liu, Y.-W. Chen, X. Liu, J.-L. Kuo, M.-W. Chu, C.-Y. Mou, *ACS Catal.* **2016**, *6*, 115–122.

[16] a) J. C. Wang, P. Liu, X. Z. Fu, Z. H. Li, W. Han, X. X. Wang, *Langmuir* **2009**, *25*, 1218–1223; b) M. Y. Guo, A. M. C. Ng, F. Z. Liu, A. B. Djurisic, W. K. Chan, H. M. Su, K. S. J. Wong, *J. Phys. Chem. C* **2011**, *115*, 11095–11101.

[17] a) A. F. Holleman, E. Wiberg, *Inorg. Chem.* **2001**, 499–501; b) J. D. Ye, S. L. Gu, S. M. Zhu, F. S. Qin, M. Liu, W. Liu, X. Zhou, L. Q. Hu, R. Zhang, Y. Shi, Y. D. Zheng, *J. Appl. Phys.* **2004**, *96*, 5308–5310.

[18] a) Y. Lv, C. Pan, X. Ma, R. Zong, X. Bai, Y. Zhu, *Appl. Catal. B* **2013**, *138*, 26–32; b) D. Chen, Z. Wang, T. Ren, H. Ding, W. Yao, R. Zong, Y. Zhu, *J.*

Phys. Chem. C **2014**, *118*, 15300–15307; c) Z. Pei, L. Ding, J. Hu, S. Weng, Z. Zheng, M. Huang, P. Liu, *Appl. Catal. B* **2013**, *142*, 736–743; d) M. Samadi, H. A. Shivaee, A. Pourjavadi, A. Z. Moshfegh, *Appl. Catal. A* **2013**, *466*, 153–160.

[19] J. Wang, Z. Wang, B. Huang, Y. Ma, Y. Liu, X. Qin, X. Zhang, Y. Dai, *ACS Appl. Mater. Interfaces* **2012**, *4*, 4024–4030.

[20] N. Uekawa, J. Kajiwara, N. Mochizuki, K. Kakegawa, Y. Sasaki, *Chem. Lett.* **2001**, *30*, 606–607.

[21] a) N. Uekawa, N. Mochizuki, J. Kajiwara, K. Kakegawa, F. Mori, Y. J. Wud, K. Kakegawa, *Phys. Chem. Chem. Phys.* **2003**, *5*, 929–934; b) B. Chavillon, L. Cario, A. Renaud, F. Tessier, F. Cheviré, M. Boujtita, Y. Pellegrin, E. Blart, A. Smeigh, L. Hammarström, F. Odobel, S. Jobic, *J. Am. Chem. Soc.* **2012**, *134*, 464–470.

[22] Y. Peng, Y. Wang, Q.-G. Chen, Q. Zhu, A. W. Xu, *CrystEngComm* **2014**, *16*, 7906–7913.

[23] S. G. Ullattil, P. Periyat, B. Naufal, M. A. Lazar, *Ind. Eng. Chem. Res.* **2016**, *55*, 6413–6421.

[24] S. A. Ansari, M. M. Khan, S. Kalathil, A. Nisar, J. Lee, M. H. Cho, *Nanoscale* **2013**, *5*, 9238–9246.

[25] a) D. Liu, Y. Lv, M. Zhang, Y. Liu, Y. Zhu, R. Zong, Y. Zhu, *J. Mater. Chem. A* **2014**, *2*, 15377–15388; b) H.-L. Guo, Q. Zhu, X.-L. Wu, Y.-F. Jiang, X. Xie, A.-W. Xu, *Nanoscale* **2015**, *7*, 7216–7223; c) X. Bai, L. Wang, R. Zong, Y. Lv, Y. Sun, Y. Zhu, *Langmuir* **2013**, *29*, 3097–3105; d) G. R. Dillip, A. N. Banerjee, V. C. Anitha, B. D. P. Raju, S. W. Joo, B. K. Min, *ACS Appl. Mater. Interfaces* **2016**, *8*, 5025–5039.

[26] A. K. Giri, C. Charan, A. Saha, V. K. Shahi, A. B. Panda, *J. Mater. Chem. A* **2014**, *2*, 16997–17004.

[27] a) V. Housková, V. Stengl, S. Bakardjieva, N. Murafa, A. Kalendová, F. Oplustil, *J. Phys. Chem. A* **2007**, *111*, 4215–4221; b) X. Zhao, M. Li, X. Lou, *Mater. Sci. Semicond. Process.* **2013**, *16*, 489–494.

[28] C. C. Hung, W. T. Lin, K. H. Wu, *J. Nanosci. Nanotechnol.* **2011**, *11*, 11190–11194.

[29] F. Chen, C. Qin, Y. Cui, N. Jiao, *Angew. Chem. Int. Ed.* **2011**, *50*, 11487–11491; *Angew. Chem.* **2011**, *123*, 11689–11693.

[30] a) V. Aureggi, G. Sedelmeier, *Angew. Chem. Int. Ed.* **2007**, *46*, 8440–8444; *Angew. Chem.* **2007**, *119*, 8592–8596; b) J. Bonnamour, C. Bolm, *Chem. Eur. J.* **2009**, *15*, 4543–4545; c) L. Lang, B. Li, W. Liu, L. Jiang, Z. Xu, G. Yin, *Chem. Commun.* **2010**, *46*, 448–450; d) M. L. Kantam, K. B. S. Kumar, C. Sridhar, *Adv. Synth. Catal.* **2005**, *347*, 1212–1214.

[31] a) Z. P. Demko, K. B. Sharpless, *J. Org. Chem.* **2001**, *66*, 7945–7950; b) F. Himo, Z. P. Demko, L. Noodleman, K. B. Sharpless, *J. Am. Chem. Soc.* **2003**, *125*, 9983–9987; c) V. Rama, K. Kanagaraj, K. Pitchumani, *J. Org. Chem.* **2011**, *76*, 9090–9095.

[32] A. K. Giri, C. Charan, S. C. Ghosh, V. K. Shahi, A. B. Panda, *Sens. Actuators B* **2016**, *229*, 14–24.